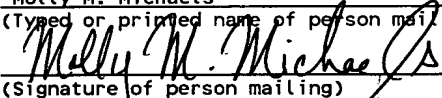


PATENT
ATTORNEY DOCKET NO. 12-1120
CERTIFICATE OF MAILING BY "EXPRESS MAIL"

"Express Mail Mailing Label Number
ET 167227295 US

Date of Deposit April 23, 2001
I hereby certify that this paper or fee is
being deposited with the United States Postal
Service "Express Mail Post Office to Addressee"
Service under 37 CFR §1.10 on the date
indicated above and is addressed to the
Commissioner of Patents and Trademarks,
Washington, D.C. 20231.

Molly M. Michaels
(Typed or printed name of person mailing)

(Signature of person mailing)

**SEMI-PHYSICAL MODELING OF HEMT HIGH FREQUENCY SMALL-
SIGNAL EQUIVALENT CIRCUIT MODELS**

Cross-Reference to Related Applications

[0001] This application is a continuation-in-part of and claims priority of U.S. patent application serial No. 60/200,666, filed on April 28, 2000.

[0002] This application is related to the following commonly-owned co-pending patent application, Serial No. 09/680, 339, filed on October 5, 2000: METHOD FOR UNIQUE DETERMINATION OF FET EQUIVALENT CIRCUIT MODEL PARAMETERS, by Roger Tsai. This application is also related to the following commonly-owned co-pending patent applications all filed on April 28, 2000, S-PARAMETER MICROSCOPY FOR SEMICONDUCTOR DEVICES, by Roger Tsai, Serial No. 60/200,307, (Attorney Docket No. 12-1114); EMBEDDING PARASITIC MODEL FOR PI-FET LAYOUTS, by Roger Tsai, Serial No. 60/200,810, (Attorney Docket No. 12-1116); SEMI-PHYSICAL MODELING OF HEMT DC-TO-HIGH FREQUENCY ELECTROTHERMAL CHARACTERISTICS, by Roger Tsai, Serial No. 60/200,648, (Attorney Docket No. 12-1118); SEMI-PHYSICAL MODELING OF HEMT HIGH FREQUENCY NOISE EQUIVALENT CIRCUIT MODELS, by Roger Tsai, Serial No. 60/200,290, (Attorney Docket No. 12-1119); HYBRID SEMI-PHYSICAL AND DATA FITTING HEMT MODELING APPROACH FOR LARGE SIGNAL AND NON-LINEAR MICROWAVE/MILLIMETER WAVE CIRCUIT CAD, by Roger Tsai and Yaochung Chen, Serial No. 60/200,622, (Attorney Docket No. 12-1127; and PM²: PROCESS PERTURBATION TO MEASURE MODEL METHOD

FOR SEMICONDUCTOR DEVICE TECHNOLOGY MODELING, by Roger Tsai,
Serial No. 60/200,302, (Attorney Docket No. 12-1128).

TECHNOLOGY MODELING

BACKGROUND OF THE INVENTION

1. Field of the Invention

[0003] The present invention relates to a method for modeling semiconductor devices and more particularly to a method for modeling semiconductor devices, such as field effect transistors (FET) and high electron mobility transistors (HEMT) for relatively accurately determining the physical device characteristics and small-signal characteristics to enable the high frequency performance of the device to be forecasted.

2. Description of the Prior Art

[0004] HEMT technology provides unparalleled, high-performance characteristics at high frequencies (microwave to millimeter wave). As such, HEMTs are used in various RF applications. In order to accurately forecast the performance of such devices it is necessary accurately model the effect of the components physical structure on its high frequency small signal characteristic. Thus, it is necessary to know how physical changes to the device will effect device performance in order to determine what process changes may be acceptable to improve RF yield product and which may be unacceptable which decrease yield.

[0005] Physical changes in such devices are known to occur as a result of various uncontrolled process events, manufacturing equipment changes or intentional process enhancement. Currently two methods for modeling the small signal characteristics of HEMT devices are known: equivalent circuit modeling; and physical device simulation.

Equivalent circuit modeling utilizes networks of linear electrical elements to model the small signal performance of the device. In the case of HEMT devices, a typical equivalent circuit topology is shown in FIG. 1. This equivalent circuit model is known to accurately model measured S-parameters (small signal characteristics) of HEMT devices up to 120 GHz.

[0006] Unfortunately, there is little correlation between the topology of the equivalent circuit and the physical structure of the device. The rough correlation of each equivalent circuit element to a location and function within a typical HEMT structure is shown in FIG. 2. As such, the small signal models are known to perform well at modeling measured S-parameters but usually contain model elements that drastically diverge from known physical quantities and characteristics. These

misrepresentations of the physical device are known to manifest as violations of basic semiconductor device principles. For example, basic device laws dictate that small signal model parameters “scale” in a predictable manner as the periphery is changed. However, most models produced by conventional means become less and less accurate as scaling is applied. As discussed above, small signal characteristics can also be simulated directly from physical device simulators. Such physical device simulators utilize comprehensive data about material characteristics and the basic device physics to simulate the actual physical location and structure of HEMT devices. Such simulators are known to be based upon finite element and Monte Carlo approaches. Such analytical tools are adapted to accept input in the form of the device physical structure, as generally shown in FIGS. 3, 4 and 5. In particular, these figures show the typical cross section and the “epi” stack used for physical simulation of specific device structures. In particular, FIG. 3 illustrates a rough scale drawing of a cross section of an exemplary HEMT device. FIG. 4 illustrates how the cross section of information regarding device structure is input into a known physical device simulator tool, such as APDS 1.0 by Agilent. FIG. 5 illustrates how the epi stack information is input into the physical device simulator. FIG. 6 illustrates where the epi stack physically resides within the total device structure.

[0007] Since these tools use a physical structure to simulate performance, the correspondence between simulated small signal performance and the device’s physical characteristics are relatively strong. However the ability of the device simulators to accurately model real measured small signal characteristics is relatively inaccurate. An example of such results is shown below in Table 1 which provides a comparison of the extracted equivalent circuit model elements using equivalent circuit modeling of measured S-parameter data and the results as modeled using a physical device simulator, for example, using APDS 1.0.

Table 1
Comparison of Modeled Equivalent Circuit Results from Prior Art Methods

Intrinsic Equivalent Circuit Parameter	Equivalent Circuit Model	Physical Device Simulator
Cgs	0.227745 pF	0.1619 pF
Rgs	64242 Ω	infinite Ω
Cgd	0.017019 pF	0.01019 pF
Rgd	133450 Ω	infinite Ω
Cds	0.047544 pF	0.044823 pF
Rds	160.1791 Ω	736 Ω
Gm	135.7568 mS	66 mS
Ri	3.034 Ω	2.304 Ω
Tau	0.443867 pS	1.433 pS

[0008] As such, there is a need for a relatively accurate method for relating known physical characteristics of a HEMT device to its measured small signal characteristics. Specifically accurate methods are needed for producing small signal models that are consistent for: measured to model accuracy; physical properties; periphery scaling and bias dependence.

SUMMARY OF THE INVENTION

[0009] Briefly the present invention relates to a semi-physical device model that can represent known physical device characteristics and measured small signal characteristics relatively accurately. The semi-physical device model in accordance with the present invention uses analytical expressions to model the fundamental electric charge and field structure of a HEMT internal structure. These expressions are based on the device physics but are in empirical form. In this way, the model is able to maintain physical dependency with good fidelity while retaining accurate measured-to-modeled small signal characteristics. The model in accordance with the present invention provides model elements for a standard small signal equivalent circuit model of FET. The model elements are derived from small signal excitation analysis of intrinsic charge and electric field as modeled within the device by the semi-physical HEMT model. As such, the RF performance can be predicted at arbitrary bias points.

DESCRIPTION OF THE DRAWINGS

[0010] These and other advantages of the present invention will be readily understood with reference to the following specification and attached drawings wherein:

[0011] FIG. 1 is schematic diagram of an exemplary small signal equivalent circuit model for a HEMT device.

[0012] FIG. 2 is a sectional view of an exemplary HEMT illustrating the rough translation of the physical origins for each of the equivalent circuit elements illustrated in the small signal circuit model in FIG. 1.

[0013] FIG. 3 is a cross-sectional view of a HEMT illustrating the regions in the HEMT which correspond to the various circuit elements in the small signal equivalent circuit model illustrated in FIG. 1.

[0014] FIG. 4 is an example of a cross-sectional descriptive input of a physical HEMT device structure by a conventional physical device simulation tool.

[0015] FIG. 5 is an example of an epi stack descriptive input of a physical HEMT device structure for a known physical device simulation tool.

[0016] FIG. 6 is an example illustrating the location of the epi stack within the device structures cross-sectional view.

[0017] FIG. 7 is an example of a relatively accurate measured-to-model I-V characteristics using the semi-physical modeling method in accordance with the present invention.

[0018] FIG. 8 is a elevational view illustrating an epi stack for an exemplary HEMT.

[0019] FIG. 9 is a cross-sectional view of a HEMT for the exemplary epi stack illustrated in FIG. 8.

[0020] FIG. 10 is a blown up diagram of the cross-sectional parameters pertaining to the T-gate geometry for the exemplary epi stack illustrated in FIG. 8.

[0021] FIG. 11 is a diagram of an electric conductance model used in the semi-physical example.

[0022] FIG. 12 is a Smith chart illustrating the measured vs modeled S-parameters S11, S12 and S22 simulated in accordance with the method in accordance with the present invention.

- [0023] FIG. 13 is similar to FIG. 12 and illustrates the measured vs. modeled values for the S21 parameter.
- [0024] FIG. 14 is similar to FIG. 12 but for the S12 S-parameter.
- [0025] FIG. 15 is a graphical illustration of the semi-physically modeled vs measured small signal Gm.
- [0026] FIG. 16 is a graphical illustration of the semi-physically simulated bias dependence of the small-signal output conductance Rds.
- [0027] FIG. 17 is a graphical illustration of the semi-physically simulated bias dependence of the small signal gate-source and gate-drain capacitance Cgs and Cgd.
- [0028] FIG. 18 is a graphical illustration of the semi-physically simulated bias-dependence of the small signal gate source charging resistance Ri.
- [0029] FIG. 19 is a graphical illustration of the semi-physically bias dependence of the small signal source and drain resistance Rs and Rd.
- [0030] FIG. 20 is a graphical illustration of the measured vs modeled bias dependent gain at 23.5 Ghz for a K-band MMIC amplifier.
- [0031] FIG. 21A and 21B are graphical illustrations of the extracted parameters from measured device I-V's for process control monitor testing.
- [0032] FIG. 22 is a graphical illustration of the measured vs semi-physically simulated process variation for Gmpk and Vgspk.
- [0033] FIG. 23 is a graphical illustration of the measured vs semi-physically simulated process variation for Idpk and Gmpk.
- [0034] FIG. 24 is a graphical illustration of the measured vs semi-physically simulated process variation for I_{max} and V_{po}.
- [0035] FIG. 25 is a graphical illustration of the measured/extracted vs semi-physically simulated process variation for the small signal equivalent model Rds and Gm.
- [0036] FIG. 26 is a graphical illustration of the measured/extracted vs semi-physically simulated process variation for the small signal equivalent model Cgs and Gm.
- [0037] FIG. 27 is a graphical illustration of the measured vs semi-physically simulated physical dependence for I_{max} as a function of physical gate length.

[0038] FIG. 28 is a graphical illustration of the measured/extracted model vs semi-physically simulated physical dependence for R_{ds} as a function of physical recess undercut width.

DETAILED DESCRIPTION

[0039] The present invention relates to a semi-physical device model which can be used to simulate RF performance through physically-based device models. The semi-physical model is an analytical model based upon empirical expressions that model the physics of HEMT operation, hence the terminology "semi-physical". The model incorporates real process parameters, such as gate length recess, etch depth, recess undercut dimensions, passivation nitride thickness, and the like. By using empirical expressions, the semi-physical model is able to maintain relatively good measured to modeled accuracy while accounting for the effects of process variations on the device performance.

[0040] The semi-physical model in accordance with the present invention provides model elements for the standard small signal equivalent circuit model or FET as illustrated in FIG. 1. However, unlike conventional methods, the model elements are derived from small signal excitation analysis of the intrinsic charge and electric fields within the device. As such, the simulated small signal model elements represent a relatively accurate physical equivalent circuit description of a physical FET.

[0041] The general methodology for the semi-physical modeling of intrinsic charge, electric conductance and electrical field is as set forth below. First, the relationships between the conduction band offsets and electrical permittivities and material composition for the various materials in the epi stack are determined. These relationships can be performed analytically or by fitting simulated data from physical simulators. Subsequently, the basic electron transport characteristics in any of the applicable bulk materials in the epi stack are determined. Once the electron transport characteristics are determined, the undepleted linear channel mobility is determined either through material characterization or physical simulation. Subsequently, the Schottky barrier height value or expressions are determined. Once the Schottky barrier height value is determined, the semi-physical equations are constructed modeling the following characteristics:

- [0042] Fundamental-charge control physics for sheet charge in the active channel as controlled by the gate terminal voltage.
- [0043] Average centroid position of the sheet charge within the active channel width.
- [0044] Position of charge partitioning boundaries as a function of gate, drain and source terminal voltages.
- [0045] Bias dependence of linear channel mobility and surface depleted regions.
- [0046] Bias dependence of the velocity saturating electric field in the channel.
- [0047] Saturated electron velocity.
- [0048] Electrical conductance within the linear region of the channel, under the gate.
- [0049] Electrical conductance within the source and drain access regions.
- [0050] Once the semi-physical equations are determined, the empirical terms of the semi-physical modeling equations are adjusted to fit the model I-V (current voltage) characteristics against measured values. Subsequently, the empirical terms are interactively readjusted to achieve a simultaneous fit of measured C-V (capacitance-voltage) and I-V characteristics. Lastly, the empirical modeling terms are fixed for future use.
- [0051] By constructing a comprehensive set of semi-physical equations that cover all of the physical phenomenon as mentioned above, the physical operating mechanisms within a HEMT device can be relatively accurately determined. FIG. 7 illustrates a set of relatively accurate measured-to-modeled I-V characteristics for a HEMT using the semi-physical modeling discussed herein. In particular, FIG. 7 illustrates the drain-to-source current I_{ds} as a function of the drain-to-source voltage V_{ds} for various gate biases, for example, from 0.4V to -1.0V. As shown in FIG. 7, solid lines are used to represent the semi-physical model while the Xs are used to represent measured values. As shown in FIG. 7, a close relationship exists between the measured values and the modeled parameters.
- [0052] An example of semi-physical modeling for physical device operation in accordance with the present invention is provided below. The example utilizes an exemplary device as illustrated in FIGS. 8 and 9. Table 2 represents exemplary values for the physical cross-section dimension parameters in the model. FIG. 10 relates to a

blown up T-gate characteristic which is correlated to the parameters identified in Table 2.

Table 2
Values for the Physical Dimension Parameters Input into Device Cross Section

	Layout Parameter	Units	Value
	Gate Length Lg	[μm]	0.150
	Wing Length Lgw	[μm]	0.520
	Gate Mushroom Crown Length Lgmcl	[μm]	0.200
	Total Gate Height Hg	[μm]	0.650
	Gate Stem Height Hgstern	[μm]	0.300
	Gate Sag Height Hgsag	[μm]	0.100
	Gate Cross-Sectional Area GateArea	[μm^2]	0.187
	Max Cross-Sectional Area MaxArea	[μm^2]	0.364
	Total Gate Periph Wg	[μm]	200.000
	# Fingers N	[]	4.000
	Source-Drain Spacing Dsd	[μm]	1.800
	Gate-Source Spacing Dsg	[μm]	0.700
	Gate-Drain Spacing Dgd	[μm]	1.100
	Gate-Source Recess RECsg	[μm]	0.160
	Gate-Drain Recess RECgd	[μm]	0.240
	Recess Etch Depth Hrec	[\AA]	780.000
	SiN Thickness Hsin	[\AA]	750.000
	Gatefeed-Mesa Spacing Dgfm	[μm]	2.000
	Gateend-Mesa Overlap Dgem	[μm]	2.000
	Finger-Finger Spacing Thru Drain Dffd	[μm]	16.500
	Finger-Finger Spacing Thru Source Dffs	[μm]	13.500
	Source Airbridge Inset? AB?	[]	P
	Source Airbridge Inset Dsabin	[μm]	28.000
	Source Airbridge Height Hsab	[μm]	3.500
	Source-Gate Airbridge Clearance Hgsab	[μm]	1.640
	Source Pad Width Ws	[μm]	12.000
	Drain Pad Width Wd	[μm]	14.000
	Substrate Thickness Hsub	[μm]	100.000

[0053] As mentioned above, the semi-physical modeling of the intrinsic charge and electric field within the HEMT device is initiated by determining the relationships between the conduction band offset, electrical permittivities and material composition for the various materials in the epi stack. Material composition related band offset and electrical permittivity relationships may be obtained from various references, such as “Physics of Semiconductor Devices,” by Michael Shur, Prentice Hall, Englewood Cliffs, New Jersey 1990. The basic electron transport characteristics, for example, for the linear mobility of electron carriers in the bulk GaAs cap layer may be determined to be $1350\text{cm}^2/\text{Vs}$, available from “Physics of Semiconductor Devices”, supra. The linear mobility of electron carriers in the undepleted channels is assumed to be

5500cm²/Vs. This value may be measured by Hall effect samples which have epi stacks grown identically to the stack in the example, except for some differences in the GaAs cap layer. The Schottky barrier height is assumed to be 1.051 volts, which is typical of platinum metal on a AlGaAs material.

[0054] The following equations represent the semi-physical analytical expressions to model the charge control and centroid position in the sample.

Empirical Charge Control Expression	N_s	[cm ²]	$= \frac{N_s'}{[1+(N_s'/N_{max})^\gamma]^{1/\gamma}}$
Ideal Charge Control with Filling Law	N_s'	[cm ²]	$= 2 N_o \ln [1+\exp(V_{gt} / (\eta V_{th}))]$
Ideal Charge Control	N_o	[cm ²]	$= \epsilon_i \eta V_{th} / [2 q (d_i + \Delta d_i) 10000]$
Maximum Channel Charge	N_{max}	[cm ²]	$= (N_{max0} + N_{maxL} V_{ds}^{nnmax}) / (H_{chan} / H_{chanREF})$
Initial Gate-Channel Voltage	V_{gt}	[V]	$= V_{gs} - \Phi_b - \Delta E_C - V_{TO} - \sigma V_{ds}$
Threshold Voltage	V_{TO}	[V]	$= \Phi_b - \Delta E_C - V_T$
Doping Threshold Voltage	V_T	[V]	$= q N_{s\delta} d\delta 10000 / \epsilon_i$
Gate-to-Channel Spacing	d_i	[m]	$= ((H_{space} + H_{bar} + H_{fdope} + H_{cap}) - H_{rec}) / (10^{10})$
note that the expression for di can be changed for different epi-stacks			
Movement of Sheet Carrier Centroid	Δd_i	[m]	$= H_{chan} [1 - d_{ik} V_{gto} / H_{chanREF} - d_{il} V_{ds} / H_{chanREF}]$
Empirical Charge Control Shaping Parameter	γ	[]	
Semi-Physical Subthreshold Populating Rate	η	[]	
Dielectric Permittivity of the Barrier Layer	ϵ_i	[F/m]	
The thermal voltage	V_{th}	[V]	$= K_B T_{amb} / q$
Ambient Temperature	T_{amb}	[K]	
Fixed Emprical Maximum Sheet Charge	N_{max0}	[cm ²]	
Vds Dependent Emprical Maximum Sheet Charge	N_{maxL}	[cm ²]	
Vds Dependent Emprical Nmax shaping term	n_{Nmax}	[]	
Channel Layer Thickness	H_{chan}	[A]	
Reference Channel Layer Thickness	$H_{chanREF}$	[A]	
(Channel Thickness for the sample for which the model was first derived)			
Schottky Barrier Height	Φ_B	[V]	
Conduction Band Offset between Channel and Barrier	ΔE_C	[V]	
Front Delta Doping	$N_{S\delta}$	[cm ²]	
note that this expression can be modified for non-delta doped epi-stacks			
Gate-to-Front Delta Doping Spacing	$d\delta$	[m]	$= ((H_{bar} + H_{fdope} + H_{cap}) - H_{rec}) / (10^{10})$
Barrier Thickness between front doping and channel	H_{space}	[A]	
Barrier Layer Thickness before front doping layer	H_{bar}	[A]	
Front Doping layer thickness	H_{fdope}	[A]	
Cap layer thickness	H_{cap}	[A]	
Empirical Drain-Induced Barrier-Lowering Term	σ	[]	
Sheet Charge Position Gate Bias Factor	d_{ik}	[A/V]	
Sheet Charge Position Drain Bias Factor	d_{il}	[A/V]	
Effective Gate Voltage	V_{gto}	[V]	$= V_{th} [1 + V_{gt}/2V_{th} + \text{sqrt}(\delta^2 + (V_{gt}/2V_{th} - 1)^2)]$
Empirical Transition Width Parameter	δ	[]	

[0055] As used herein, N_s represents the model sheet carrier concentration within the active channel. N_s' represents the ideal charge control law and is modeled as a semi-physical representative of the actual density of state filling rate for energy states

within the channel v. gate voltage. The gate-to-channel voltage used for the charge control, V_{gt} , is a function of the Schottky barrier height, conduction band offsets and doping in the epi stack as is known in the art. The following equations represent the semi-physical expression used to model the position of regional charge boundaries within the HEMT device. These expressions govern how to partition the model charge between the influence of different terminals.

Effective Gate Length	L_{goff}	[μm]	$= L_g + \Delta L_s + \Delta L_d$
Gate-Source Control Region	L_{gs}	[μm]	$= L_g/2 + \Delta L_s + X_{D1}$
Source-Side Effective Gate Length Extension	ΔL_s	[μm]	$= \Delta L_{s0} + \Delta L_K \cdot V_{gts}$
Drain-Side Effective Gate Length Extension	ΔL_d	[μm]	$= \Delta L_{d0} + \Delta L_K \cdot V_{gts} + \Delta L_L \cdot V_{dsat2}$
Gate-Drain Control Region	L_{gd}	[μm]	$= (L_g/2 + \Delta L_d) \cdot \{ \tanh [10(L_g/2 - X_{D1})] + 1 \} / 2$
Bias Dependent Extension of the Saturated Transport Region	X_{D1}	[μm]	$= X_{DL} V_{ds} M_{Xdl} /$ $\{ M_{Xdk} V_{gts} \cdot (1 + [X_{DL} V_{ds} M_{Xdl} /$ $(M_{Xdk} V_{gts} (L_g/2 + REC_{gd}))^m]^{1/m}) \}$
Empirical Drain-Saturated Transport Boundary Factor	X_{DL}	[μm]	$= L_g V_{ds} / \{ 2 [1 + (V_{ds}/V_{satn})^m]^{1/m} \}$ $= X_{s0} \{ M_{Xs} [1 / (1 + (V_{ds}/V_{satn})^m)^{1/m}] -$ $V_{ds} m (V_{ds}/V_{satn})^{(m-1)} /$ $V_{satn} m [1 + (V_{ds}/V_{satn})^m]^{1/m} \}$
Position of the Boundary between Regions 1 and 2	X_S	[μm]	$V_{ds} M_{XsL} + V_{gts} M_{XsK} \}$
Note: Region 1 denotes the linear region, while Region 2 denotes the saturated region of the channel			
Empirical Effective Gate Length Extension Gate Bias Factor	ΔL_K	[$\mu m/V$]	
Empirical Effective Gate Length Extension Drain Bias Factor	ΔL_L	[$\mu m/V$]	
Effective Drain-Source Voltage Control-2	V_{dsat2}	[V]	$= V_{ds} / \{ 1 + (V_{ds}/V_{satn})^m \}^{1/m}$
Rough, Intrinsic Saturation Voltage	V_{satn}	[V]	$= I_{sat} / g_{chl}$ $= g_{chl} V_{gts} /$ $[1 + g_{chl} R_s + \sqrt{1 + 2g_{chl} R_s + (V_{gts}/V_L)^2}]$
Rough, Intrinsic Saturation Current Level	I_{sat}	[A]	$= (q N_s \mu_{ave} W g) / L g$
Intrinsic Conductance of the Linear Region, Under the gate	g_{chl}	[S]	$= F_s \cdot L_g$
Rough Intrinsic Saturation Voltage Level	V_L	[V]	
Empirical Knee Shaping Parameter	m	[]	
Empirical Region 2 extension Drain Bias Factor	M_{Xdl}	[]	
Empirical Region 2 extension Gate Bias Factor	M_{Xdk}	[]	
Fine Intrinsic Saturation Voltage	V_{satn}	[V]	$= I_{satcom} / g_{chl}$ $= g_{chl} V_{gts} V_L \cdot [-V_L (A + g_{chl} R_s) +$ $\sqrt{V_L^2 (A + g_{chl} R_s)^2 + V_{gts}^2 - (g_{chl} R_s V_L)^2}] /$ $[V_{gts}^2 (1 - g_{chl} R_s (V_L/V_{gts})^2)]$
Fine Intrinsic Saturation Current Level	I_{satcom}	[A]	$= X_S / L_{goff}$
Saturation Region Length Ratio	A	[]	$= L_g / 2$
Initial Starting position for Region1 & 2 Boundary	X_{s0}	[μm]	
Region1 & 2 Boundary Bias Factor	M_{Xs}	[]	
Region1 & 2 Boundary Drain Bias Factor	M_{XsL}	[]	
Region1 & 2 Boundary Drain Bias Factor	M_{XsK}	[]	

[0056] The following equations represent the semi-physical expressions used to model the bias dependence of linear channel mobility in depleted regions.

Depleted Channel Mobility	μ_{ave}	$[cm^2/V*s]$	$= \mu_{dchan} + \mu_{dK} \cdot V_{gto}$
Fixed Depleted Channel Mobility	μ_{dchan}	$[cm^2/V*s]$	
Depleted Channel Mobility Gate Bias Factor	μ_{dK}	$[cm^2/V^2*s]$	

[0057] The following equations are the semi-physical expressions used to model the bias dependence of the saturating electric field and saturation velocity.

Saturating Electric Field	F_s	$[V/\mu m]$	$= v_s / [(\mu_{sat} + \mu_{satK} V_{gto}) 10000]$
Fixed Saturating Channel Mobility	μ_{sat}	$[cm^2/V*s]$	
Saturating Channel Mobility Gate Bias Factor	μ_{satK}	$[cm^2/V^2*s]$	
Saturation Velocity	v_s	$[cm/s]$	

[0058] FIG. 11 is a schematically illustrates how electrical conductance in the source and drain access regions are modeled in the example.

[0059] The following equations describe the semi-physical expressions for the source access region conductance:

Source Access Resistance	R_S	[Ω]	$= (R_{S\text{undepCap}} + R_{S\text{Access}} + R_{S\text{Boundary}}) / W_g$
Source Access Resistance: Channel and Cap	$R_{S\text{undepCap}}$	[$\Omega \cdot \mu\text{m}$]	$= R_{\text{cont}} / RF_{\text{conf}} +$ $R_{\text{SH}} D_{\text{sg}} - (REC_{\text{sg}} + L_g / 2)$ $= R_{S\text{deplRec}}^{ON} \cdot MR_s \cdot \tanh\{ [KC_{\text{fl}} \cdot (V_{\text{gs}} - V_{\text{C}_{\text{ion}}} + V_{\text{ds}} \cdot MC_{\text{fl}}) + 1] / 2 \cdot \{ V_{\text{gs}} / 2 \cdot [1 - \tanh(KR_{sK} (V_{\text{gs}} - VR_{sOn}))] \} \cdot \{ \tanh(KR_{sSat} (V_{\text{ds}} - VR_{sKnee})) + 1 \} / 2 + R_{S\text{undepRec}} \cdot \{ \tanh(KR_{sK} (V_{\text{gs}} - VR_{sOn})) + 1 \} / 2$
Source Access Resistance: Recess and Undepleted Cap	$R_{S\text{Access}}$	[$\Omega \cdot \mu\text{m}$]	$= R_{S\text{deplRec}}^{ON} \cdot MR_s \cdot \tanh\{ [KR_{sK} \cdot V_{\text{gs}} + KR_{sL} \cdot V_{\text{ds}} + VR_{sOff}] + 1 \} / 2 \cdot \{ (1 + V_{\text{ds}} \cdot MR_{sL}) \cdot MR_{sK} \cdot [1 - \tanh(KR_{sSat} (V_{\text{ds}} - VR_{sKnee}))] \} / [2 \cdot (1 + [V_{\text{gs}} / ((1 + V_{\text{ds}} \cdot MR_{sL}) \cdot MR_{sK}))^{R_{s1}}]^{(1/R_{s2})}]$
Source Access Resistance: Crowding resistance due to conductance mismatch	$R_{S\text{Boundary}}$	[$\Omega \cdot \mu\text{m}$]	$= R_{S\text{depl}} (REC_{\text{sg}})$
Resistance of the Source Recess Access region at high on-state bias (V_{on})	$R_{S\text{deplRec}}^{ON}$	[$\Omega \cdot \mu\text{m}$]	$= R_{S\text{Hundep}} (REC_{\text{sg}})$
Resistance of the Undepleted Source Recess Access region	$R_{S\text{undepRec}}$	[$\Omega \cdot \mu\text{m}$]	$= 1 / (q N_{\text{max}} \mu_{\text{ave}})$
Uncapped, Fully Depleted Sheet Resistance	$R_{SH\text{dep}}$	[Ω/sq]	$= 1 / (1/R_{SH\text{cap}} + 1/R_{SH\text{undep}})$
Capped, Undepleted Sheet Resistance	R_{SH}	[Ω/sq]	$= F_{\text{surfUndep}} / (q N_{\text{max}} \mu_{\text{undchan}})$
Uncapped, Undepleted Sheet Resistance	$R_{SH\text{undep}}$	[Ω/sq]	$= 1 / [q N_{\text{cap}} \mu_{\text{cap}} (H_{\text{cap}} - H_{\text{capEich}})]$
Cap Sheet Resistance	$R_{SH\text{cap}}$	[Ω/sq]	
Surface Depletion Factor	$F_{\text{surfUndep}}$	{ }	
High On-state bias: Diode Turn-on voltage	V_{ON}	[V]	$= \Phi_b - \Delta E_C - \Delta E_t$
Ohmic Contact Resistance	R_{cont}	[$\Omega \cdot \mu\text{m}$]	
RF Ohmic Contact Resistance Reduction Factor	RF_{conf}	{ }	
Source Access Resistance Bias Modification Factor	MR_s	{ }	
Cf-Vds Bias Modification Factor	MC_{fl}	{ }	
Rs-Vds Bias Modification Factor	MR_{sL}	{ }	
Rs-Vgs Bias Modification Factor	MR_{sK}	{ }	
Cf-Vgs Switch point to On-state	VC_{ion}	{ }	
Cf-Vgs Bias Expansion Factor	KC_{fl}	{ }	
Rs-Vgs Switch point to On-state	VR_{sOn}	{ }	
Rs-Vgs Switch point to Off-state	VR_{sOff}	{ }	
Rs-Vds Switch point from Off-On transition	VR_{sKnee}	{ }	
Rs-Vds Bias Expansion Factor	KR_{sL}	{ }	
Rs-Vgs Bias Expansion Factor	KR_{sK}	{ }	
Rs-Vds Bias Expansion Factor @ Rs Saturation	KR_{sSat}	{ }	
Rs Bias Shaping Factor	γR_s	{ }	

[0060]

The following equations describe the drain access region conductance:



Drain Access Resistance	R_D	$[\Omega]$	$= (R_{DRF} + R_{DN})$
Drain Access Resistance, except for recess access	R_{DRF}	$[\Omega]$	$= (R_{DAccess} + R_{DundepCap} + R_{DundepRec} + R_{DSaturated}) / W_g$
Drain Recess Access Resistance	R_{DN}	$[\Omega]$	$= (R_{DRec}) / W_g$
Drain Access Resistance: Recess and Undepleted Cap	$R_{DAccess}$	$[\Omega \cdot \mu m]$	$= R_{DundepRec}^{ON} (MR_g \cdot V_{gs} + 1) [1 - \tanh\{KR_{daccK} * [V_{gs} - VR_{dOn} + V_{ds} * MR_{daccL}]\}] / 2$
Drain Access Resistance: Channel and Cap	$R_{DundepCap}$	$[\Omega \cdot \mu m]$	$= R_{cont} / RF_{conF} + (REC_{gd} + L_g / 2)$
Resistance of the Undepleted Drain Recess Access region	$R_{DundepRec}$	$[\Omega \cdot \mu m]$	$= R_{SHundep} (REC_{gd})$
Resistance of the Saturated Drain Recess Access region	$R_{DSaturated}$	$[\Omega \cdot \mu m]$	$= MR_{dSat} \cdot V_{ds} \exp\{-[V_{gs} + V_{ds} * MR_{dL} + VR_{dSatOn}]^2 / (2 VR_{dSat})\} / \{VR_{dSat} [1 + (V_{ds} / VR_{dSat})^{R_d}]^{(1/R_dA + 1/R_d)}\}$
Resistance of the Drain Recess Access region at high on-state bias (V_{on})	$R_{DdepRec}^{ON}$	$[\Omega \cdot \mu m]$	$= R_{SHdep} (REC_{gd})$
	R_{DRec}	$[\Omega \cdot \mu m]$	$= \delta_{VL} \{1 + (R_{DAccess} - R_{DundepCap}) / (2\delta_{VL})\} + \sqrt{\delta^2 + ((R_{DAccess} - R_{DundepCap}) / (2\delta_{VL}) - 1)^2}$
Drain Access Resistance Bias Modification Factor	MR_d	$[\]$	
Rd-Vds Access Bias Modification Factor	MR_{daccL}	$[\]$	
Rd-Vgs Swith point to On-state	VR_{dOn}	$[\]$	
Rd-Vgs Swith point at saturation	VR_{dSat}	$[\]$	
Rdaccess-Vgs Bias Expansion Factor	KR_{daccK}	$[\]$	
Rd-Vds Saturation Bias Modification Factor	MR_{dSat}	$[\]$	
Rd-Vds Access Resistance Bias Modification Factor	MR_{dL}	$[\]$	
Rd-Vgs Saturation Swith point to Off-state	$VR_{dSatOff}$	$[\]$	
Rd-Vgs Saturation Swith point	VR_{dSat}	$[\]$	
Rd-Vgs Saturation Swith point transition width	$VR_{dSat\sigma}$	$[\]$	
Rd Bias Shaping Factor	γ_{R_d}	$[\]$	

SEMI-PHYSICAL DETERMINATION OF SMALL-SIGNAL EQUIVALENT CIRCUITS

[0061] To derive values for the familiar small signal equivalent circuit as shown in FIG. 1, a small signal excitation analysis must be applied to the semi-physically modeled physical expressions. The method of applying such an analysis is as follows:

[0062] 1) Gate Terminal Voltage Excitation

[0063] Apply a small+/- voltage delta around the desired bias condition, across the gate-source terminals.

[0064] Equivalent circuit element $G_m = \delta(I_{ds}) / \delta(V_{gs})$ where $\delta(V_{gs})$ is mostly the applied voltage deltas, but also subtracting out that voltage which is dropped across the gate source access region, shown as R_{sCont} , $R_{sundepCap}$, $R_{sundepRec}$, $R_{sdepRec}$, and $R_{sBoundary}$ in FIG. 11, above.

[0065] Equivalent circuit element C_{gs} and C_{gd} takes the form of $\delta(N_{sn}) / \delta(V_{gs}) \cdot L_{gn}$, where $\delta(N_{sn})$ is the appropriate charge control expression, and L_{gn} is the gate source or gate drain charge partitioning boundary length.

[0066] Equivalent circuit element $R_i = L_{gs} / (C_{gs,channel} * v_s)$ where $C_{gs,channel}$ is the portion of gate source capacitance attributed to the channel only, and v_s is the saturated electron velocity.

[0067] 2) Drain Terminal Voltage Excitation

[0068] Apply a small +/- voltage delta around the same bias condition as in 1, but the delta is applied across drain source terminals.

[0069] Equivalent circuit element $R_{ds} = 1 / \{ \Delta(I_{ds}) / \Delta(V_{ds}') \}$ where V_{ds}' is mostly the applied voltage deltas, but also subtracting out voltage which is dropped over both the gate source and gate drain access regions.

[0070] Equivalent circuit element C_{ds} is taken to be the sum of the appropriate fringing capacitance. Semi-Physical models, or can take the form of $\Delta(N_{sd}) / \Delta(V_{ds}') * X_{sat}$, where N_{sd} is the charge control expression for charge accumulation between the appropriate source and drain charge boundaries, and X_{sat} is the length of the saturated region, if in saturation.

[0071] 3) On-mesa Parasitic Elements: The equivalent circuit elements, R_s and R_d are expressed by the appropriate electrical conduction models of the source and drain access regions.

[0072] The RF performance can be predicted at an arbitrary bias point.

[0073] Table 4 represents a comparison of the values for a high frequency equivalent circuit model derived from equivalent circuit model extraction from and semi-physical modeling for the sample illustrated in Table 2.

Table 3
Comparison of Modeled Equivalent Circuit Results for Semi-physical Modeling Method, and Equivalent Circuit Model Extraction

Intrinsic Equivalent Circuit Parameter	Equivalent Circuit Model	Semi-Physical Device Model
Cgs	0.227745 pF	0.182 pF
Rgs	64242 Ω	infinite Ω
Cgd	0.017019 pF	0.020 pF
Rgd	133450 Ω	infinite Ω
Cds	0.047544 pF	0.033 pF
Rds	160.1791 Ω	178.1 Ω
Gm	135.7568 mS	124 mS
Ri	3.034 Ω	2.553 Ω
Tau	0.443867 pS	0.33 pS

[0074] The results of the semi-physical modeling method produce a small-signal equivalent circuit values which are relatively more accurate than the physical device simulator in this case. Furthermore, given the differences in the parasitic embedding, treatment of the two approaches, the results given in Table 3 yield much closer results than a comparison of equivalent circuit values.

[0075] Table 4 lists the values of parasitic elements used in the model derivations. An important difference between the extracted equivalent circuit model and the semi-physically derived one is the use of Cpg and Cpd to model the effect of launch capacitance for the tested structure. This difference leads to the results of the extracted model results being slightly off from the optimum physically significant solution.

Table 4
Comparison of Modeled "Parasitic" Equivalent Circuit Results for Semi-physical Modeling Method, and Equivalent Circuit Model Extraction

Extrinsic Equivalent Circuit Parameter	Equivalent Circuit Model	Semi-Physical Device Model
Rg	1.678 Ω	1.7 Ω
Lg	0.029314 nH	0.03 nH
Rs	1.7 Ω	1.21 Ω
Ls	0.002104 nH	0.003 nH

Extrinsic Equivalent Circuit Parameter	Equivalent Circuit Model	Semi-Physical Device Model
Rd	3.309899 Ω	5.07 Ω
Ld	0.031671 nH	0.02 nH
Cpg	0 pF	0.02 pF
Cpd	0 pF	0.01 pF

[0076] As shown in FIGS. 12, 13 and 14, the modeled results that are simulated using the semi-physically derived equivalent circuit model very accurately replicate the measured high frequency, S-parameter data.

[0077] The following equations represent the small-signal excitation derivation of a small-signal equivalent circuit modeled Gm. FIG. 15. illustrates the semi-physically simulated bias equations of the small signal Gm compared to measured data.

Semi-Physically Modeled Drain-Source Current Control	I_{ds}	[A]	$= g_{ch} V_{ds} (1 + \lambda V_{ds}) / [1 + (V_{ds} / V_{dsat})^m]^{1/m}$
Small-Signal Determination of equiv. Circuit Gm value	g_{mRF}	[S]	$= dI_{ds} / d(V_{gs} - V_{sAcc})$
Source-Access voltage drop	V_{sAcc}	[V]	$= I_{dsW} * (R_{SUndepCap} + R_{SAccess} + R_{SBoundary} + R_{probes} / W_g)$
Fine Extrinsic Saturation Voltage	V_{sate}	[V]	$= I_{satcom} / g_{ch}$
Extrinsic Conductance of the Linear Region, Under the gate	g_{ch}	[S]	$= g_{chl} / [1 + g_{chl} (R_s + R_d)]$
Intrinsic Conductance of the Linear Region, Under the gate	g_{chl}	[S]	$= (q N_s \mu_{ave} W_g) / L_g$

[0078] The following equations represent the small-signal excitation derivation of Rds. FIG. 16 illustrates the semi-physically simulated bias-dependence of the small-signal Rds.

Small-Signal Determination of equiv. Circuit Rds value	R_{ds}	[Ω]	$= 1 / g_{dsRF}$
	g_{dsRF}	[S]	$= \{ dI_{ds} / d(V_{ds} - R_{probed} * I_{ds} - V_{sAcc} - V_{dAcc} - V_{dSat}) \} * r_{dsF}$
Drain-Access voltage drop	V_{DAcc}	[V]	$= I_{dsW} * (R_{DUndepCap} + R_{DUndepRec} + R_{DAccess} + R_{probed} / W_g)$
Drain-Saturated Region voltage drop	V_{DSAT}	[V]	$= I_{dsW} * (R_{DSaturated})$
External Test probe or lead resistance	R_{probed}	[Ω]	$= (RF_{rdsF} + 1) * \tanh(10 * V_{ds} - V_{th}) + 1$
High Frequency conductance dispersion factor	r_{dsF}	[1]	
High Frequency conductance dispersion	RF_{rdsF}	[1]	

[0079] The following equations may be used for the small-signal excitation derivation of Cgs and Cgd. FIG. 17 illustrates the semi-physically simulated bias-dependence of the small-signal Cgs and Cgd.

Small-Signal Determination of equiv. Circuit Cgs value	C_{gs}	[fF/ μm]	$= C_{gsf} + \beta C_{gcTot} L_{gs} \cdot \{ 1 - [(V_{saten} - V_{dse}) / (2 \cdot V_{saten} - V_{dse})]^2 \}$
	C_{gd}	[fF/ μm]	$= C_{gdf} + \beta C_{gcTot} L_{gd} \cdot \{ 1 - [V_{saten} / (2 \cdot V_{saten} - V_{dse})]^2 \}$
Parasitic Gate-Source Fringing Capacitance	C_{gsf}	[fF/ μm]	$= C_{g surf} C_{f-form1} SiNF + C_{gsfSource} + C_{gsfPad}$
Parasitic Gate-Source Fringing Capacitance	C_{gdf}	[fF/ μm]	$= C_{g surf} C_{f-form1} SiNF + C_{gdfCap} + C_{gdfPad}$
Total Specific Gate-Channel Capacitance	C_{gcTot}	[fF/ μm^2]	$= C_{gc} + C_{gcdonor}$
Specific Gate-Channel Capacitance	C_{gc}	[fF/ μm^2]	$= C_{gc} Msh_{Kchan} / \{ [1 + (N_s' / (N_0 + N_{maxOc}))^{1/\gamma_c}]^{1/\gamma_c} \}$
Effective Drain-Source Voltage Control	V_{dse}	[V]	$= V_{ds} / [1 + (V_{ds} / V_{saten})^m]^{1/m}$
Specific Gate-Donor Layer Accumulation Capacitance	$C_{gcdonor}$	[fF/ μm^2]	$= q d N_{sDonor} / d V_{gs}$
Ideal Specific Gate-Channel Capacitance	C_{gc}	[fF/ μm^2]	$= q d N_s' / d V_{gs}$
Empirical Parasitic Donor Charge Control Expression	N_{sDonor}	[cm ⁻²]	$= (N_s' + N_s) \cdot (d_i + \Delta d_i) Msh_{Kpar} \cdot V_{gto} / (d_i + \Delta d_i)$
Fringing capacitance to surface of source-access region	C_{gsurf}	[fF/ μm]	
Empirical Fringing capacitance-bias shaping expression	$C_{f-form1}$	[]	$= \{ 1 - \tanh[KC_{fk}(V_{gs} - VC_{fOn} + V_{ds} MC_{fL})] \} / 2$
Fringing capacitance to source-access region	$C_{gsfSource}$	[fF/ μm]	
Fringing capacitance to source metal pads	C_{gsfPad}	[fF/ μm]	
Fringing capacitance to drain-access Capped Region	C_{gdfCap}	[fF/ μm]	
Fringing capacitance to drain metal pads	C_{gdfPad}	[fF/ μm]	
Dielectric Coating Thickness Factor	SiNF	[]	
Specific Gate-Channel Capacitance Bias ModificationFactor	Msh_{Kcahn}	[]	
Donor Charge Bias ModificationFactor	Msh_{Kpar}	[]	
Empirical Specific Charge Control Shaping Parameter	γC	[]	

[0080] The following equations are involved in the small-signal excitation derivation of Ri. FIG. 18, which follows, shows the semi-physically simulated bias-dependence of the small-signal Ri.

Gate-Source Non-quasistatic charging resistance	$R_{ICharge}$	[$\Omega \cdot \mu\text{m}$]	$= L_{gs2} W_g / [C_{gsChan} W_g v_s]$
Gate-Channel Source Capacitance	C_{gsChan}	[fF/ μm]	$= C_{gsf} + \beta C_{gc} L_{gs} \cdot \{ 1 - [(V_{saten} - V_{dse}) / (2 \cdot V_{saten} - V_{dse})]^2 \}$

[0081] FIG. 19 below shows the semi-physically simulated bias-dependence of the on-mesa parasitic access resistances, Rs and Rd.

**EXAMPLE OF SEMI-PHYSICAL MODEL AND BIAS-DEPENDENCE
SMALL-SIGNAL SOURCE AND DRAIN RESISTANCE, RS AND RD.**

[0082] The following example verifies how the semi-physical small-signal device model is able to provide accurate projections for bias-dependent small-signal performance. In this example, the same semi-physical device model as used in the previous examples was used because the example MMIC circuit was fabricated utilizing the same HEMT device technology.

[0083] In this example, the bias-dependence small-signal gain and noise performance of a two-stage balanced K-band MMIC LNA amplifier is replicated through microwave circuit simulation using small signal and noise equivalent circuits that were generated by the semi-physical model. The results of the measured and modeled results are shown below in Table 5. As seen from these results, the semi-physical device model was able to accurately simulate the measured bias-dependent performance, even though the bias variation was quite wide.

Table 5
Measured vs. Modeled Gain NF and Gain @ 23.5 GHz for K-band MMIC LNA at
Difference Bias Conditions

Bias Condition	Measured Gain @ 23.5 GHz	Predicted Gain @ 23.5 GHz	Measured NF @ 23.5 GHz	Predicted NF @ 23.5 GHz
Vds=0.5 V 112 mA/mm	15.2 dB	15.8 dB	2.97 dB	2.77 dB
Vds=1.0 V 112 mA/mm	20.6 dB	21.0 dB	2.29 dB	2.20 dB
Vds=2.0 V 112 mA/mm	19.8 dB	20.2 dB	2.25 dB	2.15 dB
Vds=3.0 V 112 mA/mm	18.9 dB	19.1 dB	2.30 dB	2.11 dB
Vds=3.5 V 112 mA/mm	18.4 dB	18.5 dB	2.34 dB	2.18 dB
Vds=4.0 V 112 mA/mm	18.0 dB	18.0 dB	2.37 dB	2.27 dB
Vds=2.0 V 56 mA/mm	16.4 dB	18.0 dB	2.45 dB	2.21 dB
Vds=2.0 V 170 mA/mm	21.4 dB	20.9 dB	2.38 dB	2.21 dB

V _{ds} =2.0 V 225 mA/mm	22.2 dB	21.0 dB	2.65 dB	2.6 dB
V _{ds} =3.0 V 225 mA/mm	21.4 dB	20.3 dB	2.71 dB	2.61 dB
V _{ds} =3.0 V 170 mA/mm	20.5 dB	20.0 dB	2.42 dB	2.22 dB
V _{ds} =4.0 V 170 mA/mm	19.6 dB	19.2 dB	2.50 dB	2.29 dB

[0084] A plot of measured vs. modeled gain for the values listed in Table 5, above, is shown in FIG. 20.

[0085] The following example verifies how the semi-physical small-signal device model is able to provide accurate projections for physically dependent small-signal performance. In this example, the same semi-physical device model as used in the previous examples was used.

[0086] In this example, physical process variation was input into the semi-physical device model in terms of statistical variation about known averages, cross-correlation, and standard deviations. The goal of this exercise was to replicate the measured DC and small-signal device variation. The degree of accurate replication indicates the degree to which the semi-physical model is physically accurate.

[0087] Table 6 below lists the simulated, and known process variation that was used:

Table 6
Statistical Process Variation Model

<u>Parameter</u>	<u>Nominal</u>	<u>Standard Dev.</u>
Gate Length	0.15 μ m	0.01 μ m
Gate-Source Recess	0.16 μ m	0.015 μ m
Gate-Drain Recess	0.24 μ m	0.020 μ m
Etch Depth	780 Å	25 Å
Pass. Nitride Thickness	750 Å	25 Å
Gate-Source Spacing	0.7 μ m	0.1 μ m
Source-Drain Spacing	1.8 μ m	0.15 μ m

[0088] In the course of microelectronic component production, sample devices are tested in process in order to gain statistical process control monitor (PCM) data. FIGs. 21A and 21B show schematically the kind of data that is extracted and recorded from measured device I-V's during PCM testing.

[0089] Since the semi-physical device model is able to simulate I-V's, it was able to simulate the variation of I-V's due to physical process variation. These I-V's were analyzed in the same fashion to extract the same parameters that are recorded for PCM testing. Figures 22, 23, and 24 show how accurately the simulated results match with measured process variation. Figure 19 shows how the semi-physically simulated V_{gpk} and G_{mpk} match with actual production measurements. Figure 20 shows how simulated I_{dpk} and G_{mpk} match, also. Finally, FIGs. 21A and 21B show how the simulated I_{max} and V_{po} also match very well.

[0090] Small-signal S-parameter measurements are also taken in process for process control monitoring. These measurements are used to extract simple equivalent circuit models that fit the measured S-parameters. Since the semi-physical device model is able to simulate these equivalent circuit models, it was able to simulate the variation of model parameters due to physical process variation.

[0091] FIGs 25, and 26 show how accurately the simulated results match with measured/extracted process variation for the small-signal model parameters. FIG. 25 shows how the semi-physically simulated R_{ds} and G_m match very well with actual extracted model process variation

[0092] More direct and convincing evidence supporting the accurate, physical nature of the semi-physical model can be shown by comparing the dependence of simulated and measured performance to real physical variable. As shown in FIG. 27, the semi-physical model is able to very accurately reproduce the dependence of I_{max} upon gate length. In addition, the semi-physical model is also able to replicate physical dependence for high-frequency small-signal equivalent circuits. This is shown in FIG. 28, which shows that it is able to reproduce the dependence of R_{ds} with Recess undercut width.

[0093] Obviously, many modifications and variations of the present invention are possible in light of the above teachings. Thus, it is to be understood that, within the scope of the appended claims, the invention may be practiced otherwise than as specifically described above.

[0094] What is claimed and desired to be covered by a Letters Patent is as follows:

T0E2+0" 0090+860